ADAPTIVE LARGE EDDY SIMULATION AND REDUCED-ORDER MODELING

Sebastian Ullmann, Stefan Löbig, Jens Lang

Preprint, Mai 2012, Department of Mathematics, Technische Universität Darmstadt

TECHNISCHE
UNIVERSITÄT
DARMSTADT

Numerical
Analysis

Adaptive large eddy simulation and reduced-order modeling

S. Ullmann*, S. Löbig*, J. Lang*°†

* Department of Mathematics, Technische Universität Darmstadt,
Dolivostr. 15, D-64293 Darmstadt, Germany
ullmann@mathematik.tu-darmstadt.de

° Center of Smart Interfaces, Technische Universität Darmstadt,
Petersenstr. 30, D-64287 Darmstadt, Germany
sloebig@mathematik.tu-darmstadt.de

† Graduate School Computational Engineering, Technische Universität Darmstadt,
Dolivostr. 15, D-64293 Darmstadt, Germany
lang@mathematik.tu-darmstadt.de

Abstract The quality of large eddy simulations can be substantially improved through optimizing the positions of the grid points. LES-specific spatial coordinates are computed using a dynamic mesh moving PDE defined by means of physically motivated design criteria such as equidistributed resolution of turbulent kinetic energy and shear stresses. This moving mesh approach is applied to a three-dimensional flow over periodic hills at Re=10595 and the numerical results are compared to a highly resolved LES reference solution. Further, the applicability of reduced-order techniques to the context of large eddy simulations is explored. A Galerkin projection of the incompressible Navier-Stokes equations with Smagorinsky sub-grid filtering on a set of reduced basis functions is used to obtain a reduced-order model that contains the dynamics of the LES. As an alternative method, a reduced-order model of the un-filtered equations is calibrated to a set of LES solutions. Both approaches are tested with POD and CVT modes as underlying reduced basis functions.

Keywords Large eddy simulation, moving mesh method, reduced-order modeling, adaptivity

1 Introduction

Locally large solution variations are best resolved by a high concentration of mesh points there and few points in the remaining domain with less solution activity. This is especially true for modeling turbulent flows by large eddy simulations (LES). Here, the characteristic length of turbulent fluctuation varies significantly

over the physical domain, which demands for an LES-specific adaptation of the grid size to turbulent length scales.

In the first part of this work we enhance the quality of our LES by applying the moving mesh method developed by Huang and Russell [1]. This r-adaptive method moves the grid points according to a time dependent mesh moving PDE to achieve higher resolution in important areas of the domain while keeping the data structure unchanged, i.e., topology and number of degrees of freedom of the spatial discretization once chosen are kept unchanged. The significance of areas is defined via a so called monitor function, which links in a natural and smooth way the mesh adaptation process to properties of the physical solution. It is commonly designed by solution-dependent quantities of interests (QoI), which are equidistributed over the adaptively chosen grid cells of the physical domain in an integral sense.

The moving mesh method has successfully been used for the computation of a turbulent flow over periodic hills using single physical QoIs [E1, 2] and various combinations of physical QoIs [E2]. In Lang et al. [E3] a moving mesh method for two-dimensional finite element computations using mathematical QoIs has been studied.

The second part of the paper focuses on reduced-order models for incompressible flows. While in many instances, the accuracy and efficiency of a numerical flow simulation can be greatly improved by adaptive meshing, the additional speed-up promised by reduced-order techniques seems attractive especially for many-query and real-time applications. In our context, by reduced-order techniques we mean models that are obtained by a Galerkin projection of a high dimensional problem on a small set of reduced basis functions with global support, that incorporate information about the solution of the high dimensional problem. Typically, the reduced basis functions are created using snapshots which are computed beforehand with a conventional numerical code. Thus, a large `off-line' computational cost, depending on the degrees of freedom of the numerical code, is accepted in order to obtain a small `on-line' cost, depending only on the number of basis functions used for the projection.

A detailed introduction to reduced-order modeling based on the proper orthogonal decomposition (POD) is given by Holmes et al. [3]. While the original purpose of the POD method was to identify coherent structures of turbulent flows and to investigate their dynamics [4], slow progress has been made towards actually simulating turbulent flows using reduced-order models. Two reasons that perhaps contribute to that stagnation are these: Firstly, even for simple laminar flows it has been observed that Galerkin reduced-order models can converge towards spurious limit cycles [5,6]. Secondly, solutions of turbulent flows are much less amenable to data compression than laminar periodic flows, in other words, turbulent flow solutions can not be approximated well by a linear combination of a small number of snapshots. Still, we want to mention some promising results that could be achieved for three-dimensional transitional and turbulent flows: Telib et al. [7]

applied a calibrated POD to the flow in a T-mixer at $Re = 300$ and $Re = 400$, Buffoni et al. [8] simulated a three-dimensional flow around a square cylinder at $Re = 300$ and Couplet at al. [9] built a reduced-order model from snapshots of an LES of the flow past a backward facing step at $Re = 7432$. In our own work [E4] we study a reduced-order model of the flow around a cylinder at $Re = 3900$, based on Smagorinsky-LES. Wang et al. [10] present a similar approach for the flow around a cylinder at $Re = 1000$.

We compare two different methods to compute basis functions from the snapshot data: proper orthogonal decomposition and centroidal Voronoi tessellation (CVT). An introduction to the CVT method is provided by Du et al. [11]. We assess the resulting POD or CVT Galerkin reduced-order models by their ability to approximate given snapshot data. Different from the comparisons performed by Burkardt et al. [12], we apply both techniques to the laminar vortex-shedding flow around a circular cylinder, and present detailed quantifications of the model and approximation errors with respect to the number of basis functions. We derive and apply a reduced-order model for the pressure in order to extend the comparisons to the drag and lift forces acting on the cylinder. Finally, we explore techniques with which a progression towards low-dimensional modeling of the large-scale structures of turbulent flows can be made.

2 Adaptive moving meshes for large-eddy simulations

2.1 Large-eddy simulation

The spatially filtered incompressible Navier-Stokes equations are given by

$$\frac{\partial \overline{u}_i}{\partial t} + \frac{\partial}{\partial x_j}\left(\overline{u}_i \overline{u}_j\right) = -\frac{\partial \overline{p}}{\partial x_i} + \frac{\partial (2\nu \overline{S}_{ij})}{\partial x_j} - \frac{\partial \tau_{ij}}{\partial x_j} + f_i \,,$$

$$\frac{\partial \overline{u}_j}{\partial x_j} = 0,$$

where the filtered velocity and pressure are denoted by $\overline{\mathbf{u}} = (\overline{u}_1, \overline{u}_2, \overline{u}_3)^T$ and $\overline{p}$, respectively. The elements of the filtered strain rate tensor $\overline{\mathbf{S}}$ are defined by $\overline{S}_{ij} = (\partial_{x_j} \overline{u}_i + \partial_{x_i} \overline{u}_j)/2$ and ν represents the molecular viscosity. The external force is given by f_i and $\tau_{ij} = \overline{u_i u_j} - \overline{u}_i \overline{u}_j$ constitutes the subgrid-scale tensor.

To model the subgrid stresses we employ the eddy viscosity approach of Smagorinsky [13],

$$\tau_{ij} \approx -2\nu_t \overline{S}_{ij} + \frac{1}{3}\tau_{kk}\delta_{ij} \qquad \text{with} \qquad \nu_t = \left(C_S \Delta\right)^2 \left|\overline{\mathbf{S}}\right|.$$

Here, ν_t is the turbulent eddy viscosity, C_S denotes the Smagorinsky constant, Δ is the filter width and the norm of the filtered strain rate tensor is given by $|\bar{\mathbf{S}}| = (2\bar{S}_{ij}\bar{S}_{ij})^{1/2}$.

2.2 Moving mesh method

The moving mesh method developed by Huang and Russell [1] employs a time-dependent moving mesh partial differential equation (MMPDE) to move the grid points in a way such that the coordinates minimize an adaptation functional. The essential part of the functional is formed by the monitor function which controls the concentration of the mesh via some solution-dependent quantity of interest (QoI).

The MMPDE is defined as a coordinate transformation from a physical domain Ω to a computational domain Ω_c, where the coordinates are denoted by $\mathbf{x} = (x_1, \ldots, x_n)^T$ and $\boldsymbol{\xi} = (\xi_1, \ldots, \xi_n)^T$, respectively. For actual computations, however, it is more convenient to have the MMPDE in the non-conservative formulation for the inverse mapping $\mathbf{x} = \mathbf{x}(\boldsymbol{\xi}, t)$,

$$\tau \frac{\partial \mathbf{x}}{\partial t} = P \left[\sum_{i,j} \underbrace{\nabla \xi_i^T G^{-1} \nabla \xi_j}_{a_{ij}} \frac{\partial^2 \mathbf{x}}{\partial \xi_i \partial \xi_j} - \sum_i \underbrace{\sum_j \nabla \xi_i^T \frac{\partial G^{-1}}{\partial \xi_j} \nabla \xi_j}_{b_i} \frac{\partial \mathbf{x}}{\partial \xi_i} \right],$$

since the location of the mesh points is then defined explicitly. The parameter τ is used to adjust the time-scale of the mesh movement and is usually held fixed during the computation. For large values of τ, the mesh movement is smoother and therefore the MMPDE is easier to integrate numerically, whereas a smaller value results in faster adaption of the mesh to changes of the monitor function G. The parameter P is used to achieve a spatially balanced MMPDE and is often chosen as some bound on the coefficients, i.e.,

$$P = \frac{1}{\sqrt{\sum_i (a_{ii}^2 + b_i^2)}}.$$

As suitable boundary condition for our MMPDE we move the boundary points by extrapolating their position from interior cells in such a way that we obtain orthogonal cells.

The monitor function G in the MMPDE is a positive definite and symmetric $n \times n$ matrix and also the heart of the moving mesh method. It contains some quantity of interest (QoI) that is responsible for the assignment of important areas since the MMPDE equidistributes the product of the QoI and the cell volume over the domain. These QoI can be mathematically or physically motivated, like error

indicators or the solution's gradient. A common choice is Winslow's monitor function [14] together with an intensity parameter γ

$$G = \omega I, \qquad \omega = \sqrt{1+\gamma \|\psi\|^2}.$$

We use this as basis for constructing our monitor function for multiple QoIs. Our technique is related to the concept of the balanced monitor function (BMF) by van Dam [15]. The resulting monitor function reads

$$G = \omega \mathbf{I},$$
$$\omega(\boldsymbol{\psi}) = 1+\gamma \sum_{p=1}^{N_p} g_p \omega_p(\boldsymbol{\psi}) = 1+\gamma \sum_{p=1}^{N_p} g_p \left[\frac{(1-\beta)\alpha_p + \beta\psi_p}{(1-\beta)\alpha_p + \beta M_p} \right].$$

Here, $\psi = (\psi_1, \ldots, \psi_{N_p})^T$ is the vector of N_p different QoI, α_p and M_p are the corresponding average and maximum values, respectively. We normalize each QoI with its maximum value to ensure that all are at least approximately of the same range. The additional normalization of each QoI by its respective average prevents single large maximum values from dominating all other monitor values on the rest of the domain. Additionally, weights g_i with sum one are introduced that can be assigned to the different QoIs.

The monitor function is usually very non-smooth and therefore we apply a local averaging technique. This leads to smoother meshes and reduces the stiffness of the MMPDE. A description of the smoothing technique can be found in Hertel et al. [E2].

2.3 Numerical realization

To solve the three-dimensional momentum and mass conservation on moving grids the Arbitrary Lagrangian-Eulerian (ALE) Method is employed in its filtered form. The governing equations read, see Ferziger [16],

$$\frac{\mathrm{d}}{\mathrm{d}t}\int_{V(t)} \overline{u}_i \mathrm{d}V + \int_{V(t)} \frac{\partial\left[\overline{u}_i(\overline{u}_j - u_{G,j})\right]}{\partial x_j}\mathrm{d}V =$$
$$-\int_{V(t)} \frac{\partial \overline{p}}{\partial x_i}\mathrm{d}V + \int_{V(t)} \frac{\partial(2\nu \overline{S}_{ij})}{\partial x_j}\mathrm{d}V \quad - \int_{V(t)} \frac{\partial \tau_{ij}}{\partial x_j}\mathrm{d}V + \int_{V(t)} f_i \mathrm{d}V$$
$$\frac{\mathrm{d}}{\mathrm{d}t}\int_{V(t)} \mathrm{d}V + \int_{V(t)} \frac{\partial\left(\overline{u}_j - u_{G,j}\right)}{\partial x_j}\mathrm{d}V = 0\,.$$

Here, u_G and $V(t)$ are the velocity and time-dependent volume of a computational cell, respectively. When discretizing the governing equations there is a risk of introducing mass sources or sinks in the flow field when the velocity u_G and the change of volume over time are not treated consistently.

For this reason, the Geometric Conservation Law (GCL), see Demirdzic [17],

$$\frac{\mathrm{d}}{\mathrm{d}t}\int_{V(t)} \mathrm{d}V - \int_{V(t)} \frac{\partial u_{G,j}}{\partial x_j}\,\mathrm{d}V = 0$$

needs to be satisfied. The GCL is used to determine the velocity by the given change of volume of the computational cell to ensure consistency. The resulting expressions for the components of u_G are included in the discretized governing equations, so that only the change of volume over time remains, split into separate expressions for each face of the cell [17,16]. Hence, the GCL is not treated as separate equation here, but is introduced into the discrete form of the first governing equation.

In each time step, the MMPDE has to be integrated first since the described ALE formulation for the governing equations requires the new grid points at the end of the time step to evaluate the change of volume over time for each cell. Central Finite Differences in space together with an implicit time scheme are used for the discretization of the MMPDE. It is sufficient to solve the MMPDE up to moderate accuracy since not the exact position of the grid points but just an appropriate direction for moving the grid points with a suitable velocity is needed and therefore the implicit Euler scheme is adequate. To use the implicit Euler scheme, the coefficients a_{ij} and b_i in the MMPDE are frozen during the time step, i.e., they are only once determined at the starting time. The strongly implicit procedure (SIP) introduced by Stone [18] is used to solve the resulting system of equations. The MMPDE approach has been successfully implemented in the LESOCC2 code [2, E2], which is used for numerical tests in the following.

2.4 Turbulent flows over periodic hills

The turbulent flow through a channel with streamwise periodically arranged constrictions was proposed as a test case for separation from curved surfaces, e.g. in Fröhlich et al. [19]. Figure 1 shows the extent of the computational domain with respect to the hill height. The coordinates x, y and z denote streamwise, normal and spanwise direction, respectively, and we have $L_x = 9h$, $L_y = 3.035h$ and $L_z = 4.5h$. The Reynolds number is $Re = 10595$, based on the hill height and the bulk velocity at the crest of the hill. The main features of this flow are a free shear layer above a recirculation area downstream of the hill, reattaching roughly at half the domain length followed by a strong acceleration at the windward side of the next hill. The resolution of the flow near the separation point has a strong impact on the reattachment of the recirculating flow as well as on the characteristics of the shear layer. The domain has periodic boundary conditions in streamwise and spanwise direction and walls on the boundaries in y-direction.

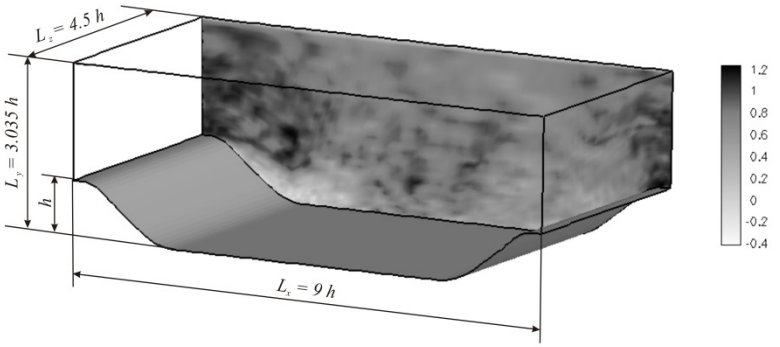

Figure 1: Geometry and computational domain for the flow over periodic hills. The contour plot at the back shows a snapshot of the instantaneous streamwise velocity u.

The reference solution for this test case is provided by Fröhlich et al. [19]. This highly resolved LES was carried out on a wall-resolving, nearly orthogonal $196\times128\times186$ grid. For our computations we use an initial grid with $89\times33\times49$ points equispaced in x-direction and equidistant grid points along each vertical line. Figure 2 illustrates the adaptation process. We begin our computation with a statistically converged LES on the initial grid. Since we want to improve the LES with respect to the statistical flow properties it is not necessary to move the grid in every time step. Instead we adapt the grid every N_{aver} time steps. During these N_{aver} time steps temporal averages (with additional average in homogeneous z-direction) are computed for use in the MMPDE. The adaptation is carried out here only in two dimensions (x, y) because of the statistically homogeneous nature of the flow with respect to the spanwise direction. The grid is adapted N_{adapt} times until it approaches a nearly steady state. Finally, a simulation on the obtained stationary grid is carried out to determine the statistics.

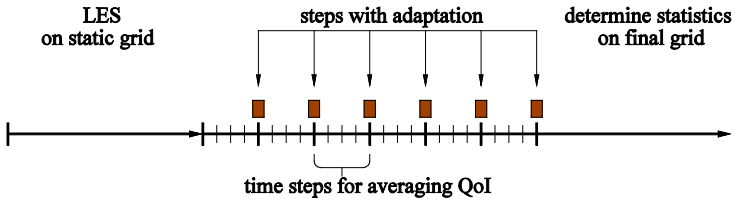

Figure 2: Illustrated outline of the adaptation procedure applied.

For the computations presented here we chose $N_{avr} = 225$, i.e., approximately a half flow through time. Tests showed that all adaptive grids in each computation of the flow over periodic hills have reached a nearly steady state after $N_{adapt} = 300$ adaptations. For the time-scaling and the intensity parameter the combination of $\tau = 1.0$ and $\gamma = 10$ lead to satisfactory results in all cases without risking overshooting grid points. Following van Dam [15], we chose $\beta = 0.3$ in the balanced monitor function.

Various physically motivated criteria for mesh movement as well as combinations of these criteria have been investigated in Hertel et al. [E2]. Some of these criteria will be introduced as well as the results of the respective computations will be presented here. Statistically averaged values were used since the focus was on the improvement of the LES with respect to statistical flow properties. In the equations below, $\langle . \rangle$ indicates averaging in time and statistically homogeneous z-direction.

The *gradient of the streamwise velocity* (GU)

$$\psi_{gu} = \left| \nabla \langle \overline{u}_1 \rangle \right|$$

is high along the hill and promises a high mesh concentration near the wall and around the separation point of the recirculation area. The gradient includes all regions of the flow field with at least one large derivative.

Equidistributing the criterion resulting from the *turbulent kinetic energy* (TKE)

$$\psi_{k,tot} = \frac{\langle k_{sgs} \rangle}{k_{tot,max}} \quad \text{with} \quad k_{tot,max} = \max_{\Omega_c} \left(\langle k_{res} \rangle + \langle k_{sgs} \rangle \right),$$

i.e., the ratio between the modeled TKE k_{sgs} of the subgrid-scales and the maximum of the total TKE over the flow field $k_{tot,max}$, over the domain is motivated by the idea of LES. The unresolved TKE is determined here via the approach by Berselli et al. [20], $k_{sgs} \approx \left(2^{1/3} - 1\right) 0.5 \left| \overline{\mathbf{u}} - \overline{\overline{\mathbf{u}}} \right|^2$. In order to avoid unphysically high values in regions where k_{res} is small, the maximum of the total TKE had to be used for the QoI instead of the local total amount of TKE.

Also motivated by the idea of LES is the balance of modeled to total *shear stress* (ST)

$$\psi_{\tau} = \frac{\langle \tau_{12}^{mod} \rangle}{\left| \langle \tau_{12}^{mod} \rangle \right| + \left| \langle \overline{u}_1'' \overline{u}_2'' \rangle \right|} \qquad \text{with} \qquad \tau_{12}^{mod} = \nu_t \left(\frac{\partial \overline{u}_1}{\partial y} + \frac{\partial \overline{u}_2}{\partial x} \right).$$

The modeled SGS shear stress is available when the Smagorinsky model is used. Refinement is needed when this value is large since then more shear stress is modeled than resolved. To avoid unphysically high values for ψ_{τ} the absolute values had to be applied in the denominator.

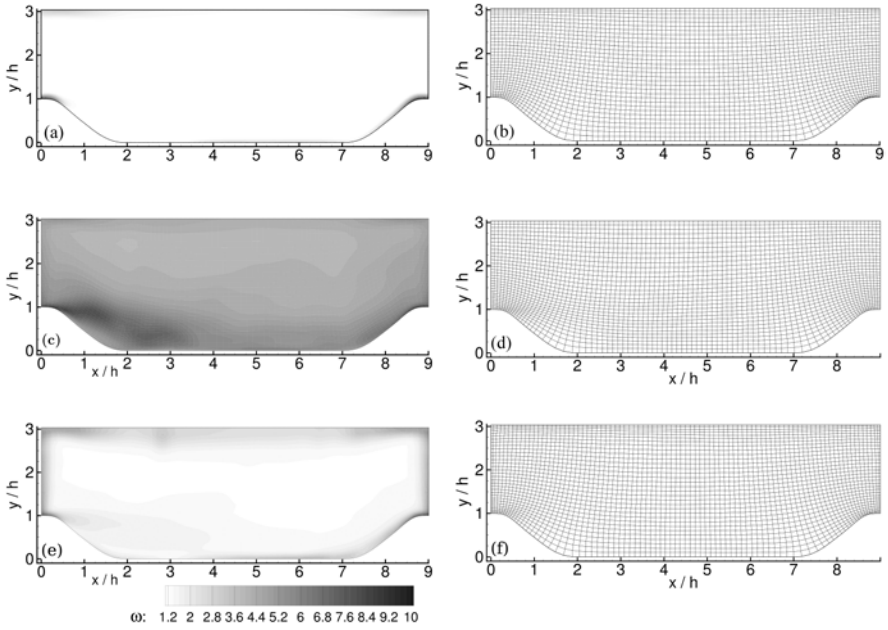

Figure 3: Left: monitor function ω. Right: final grid after 300 adaptations. QoI: (a,b) gradient of streamwise velocity; (c,d) turbulent kinetic energy; (e,f) shear stress.

Investigations on moving grids using single criteria have shown that neither TKE nor ST lead to satisfactory results for the turbulent flow over periodic hills [2, E2]. The performance of the gradient of the streamwise velocity however exceeds those of every other physically motivated criterion tested so far. Therefore, it seems natural to try to further improve the achieved quality by combining the gradient with other criteria when adapting the grid.

Figure 3 presents pictures of the monitor function and the final grid after 300 adaptations for the gradient of the streamwise velocity ψ_{gu} and the combination of the gradient with the TKE ψ_{gu} & $\psi_{k,tot}$ and the ST ψ_{gu} & ψ_{τ}.

For the gradient of the streamwise velocity the monitor function is expectedly high near the crest of the hill, especially on the windward side of the hill where a strong acceleration of the flow takes place. Also near the separation point high values of the monitor function can be observed. Moderate values are achieved near the upper wall. In the rest of the domain the monitor function is negligibly small. The grid refinement is according to the monitor values strong near the hill crest and the separation point and achieves nearly wall resolution in those regions, but only in wall normal direction. Combining the gradient of the streamwise velocity with other criteria leads to monitor functions with high values in regions where the gradient or the second criterion proposed large values. In the case of the

combination with the TKE, ψ_{gu} & $\psi_{k,tot}$, this yields high monitor values and therefore grid refinement in the free shear layer after the separation from the hill. Closer examination reveals that the refinement does not happen at the exact separation point but some small distance away from it downstream. The combination of gradient and shear stress leads to some refinement near the upper wall in addition to the crest of the hill. In the other regions of the domain the monitor function for this combination stays negligibly small.

2.5 Results

We are interested in an improvement of the statistical quality of LES. Therefore we compare our results with the reference data and our initial grid concerning the averaged streamwise velocity $\langle \overline{u}_1 \rangle$ and the Reynolds shear stress $\langle \overline{u}_1'' \overline{u}_2'' \rangle$. Figure 4 shows the mean profiles for these quantities at positions $x/h = 0.5, 4.0, 8.0$.

Significant improvement compared to the initial grid can be observed for every QoI. Although the average streamwise velocity is well predicted in position and amplitude of the maximum, the gradient and its combination with the shear stress have small problems in capturing the velocity near the bottom of the domain at $x/h = 4.0$. Greater differences in the predictions can be observed when it comes to the Reynolds shear stress. Here, the gradient of the streamwise velocity captures the amplitude of the maxima overall best despite its weakness again at $x/h = 4.0$. For $x/h = 0.5$ the combination of gradient and TKE predicts the position of the maximum Reynolds shear stress well but fails to capture the right amplitude.

The comparison of the predicted separation and reattachment points for the different QoI, see Table 1, shows how strong the gradient of the streamwise velocity already is on its own. The combination with other criteria corrupts the prediction of the separation point in both cases. Only the reattachment point is better predicted by the combination of the gradient of the streamwise velocity with the shear stress. Despite the inferior performance of the combined criteria, here each QoI improves the prediction of the initial grid considerably.

Table 1: Separation and reattachment points for different QoIs. Values obtained with final adapted grids compared to the reference data.

	Reference	Initial	ψ_{qu}	ψ_{qu} &	ψ_{qu} & ψ_{τ}
x_{sep}/h	0.20	0.53	0.29	0.40	0.37
x_{rea}/h	4.56	3.08	4.48	3.90	4.53

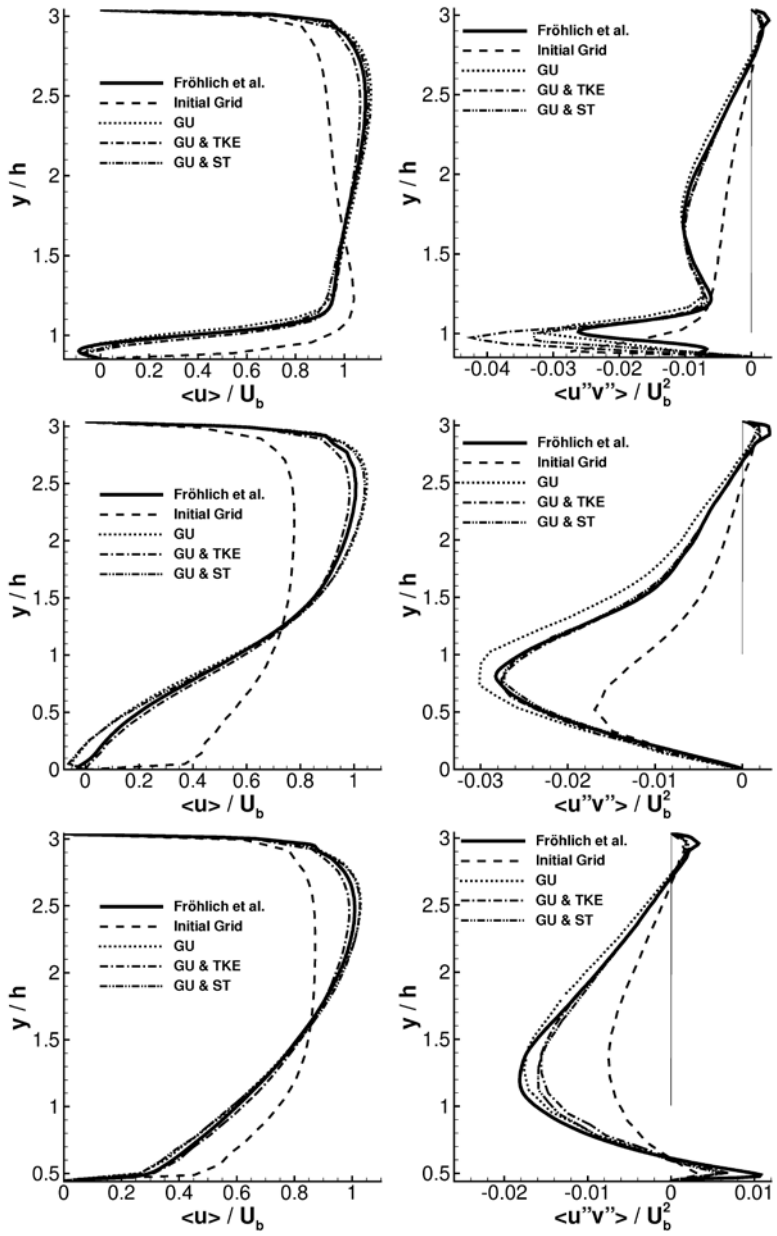

Figure 4: Averaged streamwise velocity $\langle \overline{u}_1 \rangle$ $(= \langle \overline{u} \rangle)$ and Reynolds shear stress $\langle \overline{u}_1'' \overline{u}_2'' \rangle$ $(= \langle \overline{u}'' \overline{v}'' \rangle)$ at positions $x/h = 0.5$ (top), $x/h = 4.0$ (middle) and $x/h = 8.0$ (bottom) in comparison with data from Fröhlich et al. [19] for adaptation using the following criteria: ψ_{gu}, $\psi_{gu} \& \psi_{k,tot}$ and $\psi_{gu} \& \psi_{\tau}$.

3 Reduced-order modelling

The construction of the reduced-order models is based on the following matrix form of a spatial semi-discretization of the Smagorinsky LES equations:

$$\mathcal{M}\dot{\mathbf{U}} = \mathcal{B}(\mathbf{U})\mathbf{U} + \mathcal{C}P + \mathcal{D}(\mathbf{U})\mathbf{U},$$
$$0 = \mathcal{C}^T\mathbf{U}.$$

Here, $\mathcal{M}$ is a mass matrix and $\mathcal{C}$ is a discretized gradient operator. Later on, the $\mathcal{M}$ inner product and norm,

$$(\mathbf{V},\mathbf{W})_{\mathcal{M}} = \mathbf{V}^T\mathcal{M}\mathbf{W}, \qquad \|\mathbf{V}\|_{\mathcal{M}} = (\mathbf{V}^T\mathcal{M}\mathbf{V})^{1/2},$$

respectively, will be used, which are discretizations of the L^2 inner product and norm. The advection matrix $\mathcal{B}(\mathbf{U})$ depends linearly on $\mathbf{U}$ and the viscosity matrix $\mathcal{D}(\mathbf{U})$ depends non-linearly on $\mathbf{U}$ via the turbulent viscosity. In case of a direct numerical simulation (DNS), the viscosity matrix becomes independent of the velocity.

3.1 Proper orthogonal decomposition

Let $\mathbf{U}_1,\ldots,\mathbf{U}_N$ be a set of discrete velocity snapshot vectors that are numerically obtained from a DNS or LES at time steps $t_1,\ldots,t_N$. The elements of each snapshot vector are the solution values at the mesh nodes. We define the snapshot fluctuations $\mathbf{U}'_n = \mathbf{U}_n - \bar{\mathbf{U}}$ for $n = 1,\ldots,N$ with respect to some discrete reference velocity vector $\bar{\mathbf{U}}$. In the following we present the proper orthogonal decomposition in this setting, by applying the method of snapshots [4] to the snapshot fluctuations $\mathbf{U}'_1,\ldots,\mathbf{U}'_N$. The theory is derived in Holmes et al. [3] for a more general context.

POD modes of a snapshot fluctuation matrix $\mathcal{S} = (\mathbf{U}'_1,\ldots,\mathbf{U}'_N)$ are a set of vectors $\mathbf{\Phi}_1,\ldots,\mathbf{\Phi}_R$ that satisfy $(\mathbf{\Phi}_i,\mathbf{\Phi}_j)_{\mathcal{M}} = \delta_{ij}$ for all combinations of $i, j = 1,\ldots,R$ and that solve

$$\min_{\{\mathbf{\Phi}_r\}} \sum_{n=1}^{N} \left\| \mathbf{U}'_n - \sum_{r=1}^{R} (\mathbf{U}'_n,\mathbf{\Phi}_r)_{\mathcal{M}}\mathbf{\Phi}_r \right\|^2_{\mathcal{M}} \tag{3.1}$$

for a given R that is not larger than the rank of $\mathcal{S}$. A solution of the minimization problem can be obtained by the following procedure:

- Compute the eigendecomposition $\mathcal{S}^T\mathcal{M}\mathcal{S} = \mathcal{V}\Sigma^T\Sigma\mathcal{V}^T$, where $\Sigma \in \mathbb{R}^{N\times N}$ is a diagonal matrix that contains the square roots of the (non-negative) eigenvalues $\lambda_1,\ldots,\lambda_N$ ordered non-increasingly on the diagonal and $\mathcal{V} \in \mathbb{R}^{N\times N}$ contains the corresponding eigenvectors.

- Choose an approximation rank R, not larger than the number of non-zero eigenvalues. Define $\mathcal{V}_R \in \mathbb{R}^{N\times R}$ as the matrix that contains the left R columns of $\mathcal{V}$ and define $\Sigma_R \in \mathbb{R}^{R\times R}$ as the upper left portion of Σ.
- Compute the matrix $\mathcal{U}_R = (\mathbf{\Phi}_1,\ldots,\mathbf{\Phi}_R)$ by $\mathcal{U}_R = \mathcal{S}\mathcal{V}_R\Sigma_R^{-1}$.

The POD can also be defined using singular value decomposition,

$$\mathcal{M}^{1/2}\mathcal{S} = \widehat{\mathcal{U}}\Sigma\mathcal{V}^T, \qquad \mathcal{M}^{1/2}\mathcal{U} = \widehat{\mathcal{U}}.$$

In this case $\mathcal{U}_R$ is formed by the left R columns of $\mathcal{U}$ and the matrices $\mathcal{V}_R$ and Σ_R are defined as above. This approach requires a factorization $\mathcal{M} = (\mathcal{M}^{1/2})^T\mathcal{M}^{1/2}$, so for non-diagonal mass matrices the eigendecomposition of $\mathcal{S}^T\mathcal{M}\mathcal{S}$ is the preferred method.

For the derivation of the reduced-order model it will be useful that the POD modes are a linear combination of the snapshot fluctuation vectors,

$$\mathbf{\Phi}_r = \sum_{n=1}^{N} \frac{(\mathbf{U}_n', \mathbf{\Phi}_r)_{\mathcal{M}}}{\lambda_r}\mathbf{U}_n', \tag{3.2}$$

which means that some properties of the snapshot fluctuations are carried over to the POD modes.

3.2 Centroidal Voronoi tessellation

The Centroidal Voronoi tessellation is a method that groups the set of discrete snapshot fluctuation vectors $\mathbf{U}_1',\ldots,\mathbf{U}_R'$ in clusters, such that on average the distances between each cluster's center and its members are small. More precisely, the CVT is defined as a set of clusters $V_1,\ldots,V_R$ and a set of modes $\mathbf{\Phi}_1,\ldots\mathbf{\Phi}_R$ that solve the minimization problem

$$\min_{\{\mathbf{\Phi}_r\},\{V_r\}} \sum_{r=1}^{R}\sum_{\mathbf{U}_n'\in V_r} \left\|\mathbf{U}_n' - \mathbf{\Phi}_r\right\|_{\mathcal{M}}^2. \tag{3.3}$$

The CVT of a collection of snapshot fluctuation vectors can be computed using a variant of Lloyd's method [21]:

1. Assign each vector to some cluster.
2. Handle empty clusters.
3. Compute all cluster mid-points.
4. Assign each vector to the cluster whose mid-point is closest.
5. If in step 4 any vector was shifted, then go to step 2, otherwise quit.

The CVT modes are then given by the cluster mid-points,

$$\mathbf{\Phi}_r = \frac{1}{|V_r|} \sum_{\mathbf{U}'_n \in V_r} \mathbf{U}'_n, \tag{3.4}$$

where $|V_r|$ is the number of snapshots contained in the cluster V_r. Thus, for the CVT it holds that each mode is a linear combination of snapshot fluctuation vectors.

While the POD modes are orthonormal with respect to the $\mathcal{M}$-inner product, the CVT modes are not $\mathcal{M}$-orthonormal in general. It is even possible that they are linearly dependent, in which case they do not form a linear basis. In the special case that the CVT modes are computed from a set of snapshot fluctuations with respect to the snapshot mean, the CVT modes are always linearly dependent. To prove the linear dependence we need to find a set of coefficients $a'_1,\ldots,a'_R$, not all equal to zero, for which $a'_1\mathbf{\Phi}_1 + \ldots + a'_R\mathbf{\Phi}_R = 0$. Choosing $a'_r = |V_r|$ for $r = 1,\ldots,R$, we can write for any reference flow

$$\sum_{r=1}^{R} a'_r\mathbf{\Phi}_r = \sum_{r=1}^{R} \frac{a'_r}{|V_r|} \sum_{\mathbf{U}'_n \in V_r} \mathbf{U}'_n = \sum_{n=1}^{N} (\mathbf{U}_n - \bar{\mathbf{U}}) = \Big(\sum_{n=1}^{N} \mathbf{U}_n\Big) - N\bar{\mathbf{U}}.$$

If the reference flow is the snapshot mean, it follows that

$$\Big(\sum_{n=1}^{N} \mathbf{U}_n\Big) - N\bar{\mathbf{U}} = \sum_{n=1}^{N} \mathbf{U}_n - N\Big(\frac{1}{N}\sum_{n=1}^{N} \mathbf{U}_n\Big) = 0.$$

As a consequence, a reference flow different from the snapshot mean must be used. If a stationary solution of the flow problem was available, we could use this stationary solution as a reference, as done in Burkardt et al. [12]. Otherwise we could also select a snapshot from the available solution data of the start-up phase of the simulation. Taking some snapshot $\mathbf{U}_n$ as a reference flow is not recommended, because this will lead to $\mathbf{U}'_n = 0$, which results in a zero CVT mode if $\mathbf{U}'_n$ happens to be the only member of its cluster. In any case, it is recommended to check the output of Lloyd's method for linear independence.

3.3 Reduced-order velocity model

The derivation of the Galerkin reduced-order model for the direct numerical simulation is based on the reduced basis approximation $\mathbf{U}^R$ of some discrete velocity vector $\mathbf{U}$,

$$\mathbf{U}^R = \bar{\mathbf{U}} + \sum_{r=1}^{R} a_r\mathbf{\Phi}_r \tag{3.5}$$

where $\mathbf{\Phi}_1,\ldots,\mathbf{\Phi}_R$ can be POD or CVT basis functions. We assume that the discrete velocity snapshots $\mathbf{U}_1,\ldots,\mathbf{U}_N$ fulfill the discrete continuity equation

$C^T\mathbf{U}=0$ sufficiently well. Using the properties (3.2) and (3.4) of the POD and CVT basis functions, one can verify that divergence-free snapshots imply divergence-free basis functions, $C^T\mathbf{\Phi}_r=0$ for $r=1,\ldots,R$, which imply divergence-free reduced basis approximations, $C^T\mathbf{U}^R=0$. Therefore, we concentrate solely on the discrete momentum equation

$$\mathcal{M}\dot{\mathbf{U}}=\mathcal{B}(\mathbf{U})\mathbf{U}+\mathcal{D}\mathbf{U}+\mathcal{C}P.$$

Projecting this system of equations on the reduced basis functions $\mathbf{\Phi}_1,\ldots,\mathbf{\Phi}_R$ results in

$$\mathbf{\Phi}_r^T\mathcal{M}\dot{\mathbf{U}}=\mathbf{\Phi}_r^T\mathcal{B}(\mathbf{U})\mathbf{U}+\mathbf{\Phi}_r^T\mathcal{D}\mathbf{U}+\mathbf{\Phi}_r^T\mathcal{C}P,\qquad r=1,\ldots,R. \tag{3.6}$$

Assuming that the reduced basis functions are discretely divergence-free, it holds that $\mathbf{\Phi}_r^T\mathcal{C}P=(C^T\mathbf{\Phi}_r)^TP=0$ for any $r=1,\ldots,R$. Substituting (3.5) into (3.6) leads to

$$\sum_{i=1}^{R}A_{ri}\dot{a}_i=\sum_{i,j=1}^{R}B_{rij}a_ia_j+\sum_{i=1}^{R}C_{ri}a_i+D_r\qquad r=1,\ldots,R. \tag{3.7}$$

with

$$\begin{aligned}
A_{ri}&=\mathbf{\Phi}_r^T\mathcal{M}\mathbf{\Phi}_i, && r,i=1,\ldots,R,\\
B_{rij}&=\mathbf{\Phi}_r^T\mathcal{B}(\mathbf{\Phi}_j)\mathbf{\Phi}_i, && r,i,j=1,\ldots,R,\\
C_{ri}&=\mathbf{\Phi}_r^T\mathcal{B}(\overline{\mathbf{U}})\mathbf{\Phi}_i+\mathbf{\Phi}_r^T\mathcal{B}(\mathbf{\Phi}_i)\overline{\mathbf{U}}+\mathbf{\Phi}_r^T\mathcal{D}\mathbf{\Phi}_i, && r,i=1,\ldots,R,\\
D_r&=\mathbf{\Phi}_r^T\mathcal{B}(\overline{\mathbf{U}})\overline{\mathbf{U}}+\mathbf{\Phi}_r^T\mathcal{D}\overline{\mathbf{U}}. && r=1,\ldots,R.
\end{aligned}$$

Suitable initial conditions can be derived by projecting the initial conditions of the spatial semi-discretization on the reduced basis functions. The computing time of the reduced-order system of ordinary differential equations (3.7) is only dependent on the number of basis functions R, but not on the number of mesh nodes any more.

3.4 Reduced-order pressure model

The pressure has been eliminated from the reduced-order model described in the last section. For the computation of the drag and lift coefficients, however, the pressure field is needed. In the following, we describe a way to compute the pressure from the solution of reduced-order velocity models. The method is based on the ideas of Rempfer [22] and Noack et al. [23], who substituted the reduced-order approximation of the velocity field in the right-hand side of a continuous pressure Poisson equation. We extend this method to the case of a discrete pressure Poisson equation. For details on continuous and discrete pressure Poisson equations, see Gresho and Sani [24].

The discrete pressure Poisson equation is derived by substituting the discrete momentum equations in the time derivative $\mathcal{C}^T \dot{\mathbf{U}} = 0$ of the discrete continuity equation, which yields

$$-\mathcal{C}^T \mathcal{M}^{-1} \mathcal{C} P = \mathcal{C}^T \mathcal{M}^{-1} (\mathcal{B}(\mathbf{U}) + \mathcal{D}) \mathbf{U}. \tag{3.8}$$

With this equation we can compute the pressure associated with a discrete velocity field $\mathbf{U}$. If we substitute a reduced basis approximation $\mathbf{U}^R$ of $\mathbf{U}$, see (3.5), and denote the resulting pressure by P^R, we can rewrite the discrete pressure Poisson equation (3.8) as

$$\begin{aligned} -\mathcal{C}^T \mathcal{M}^{-1} \mathcal{C} P^R = & \sum_{i,j=1}^{R} \mathcal{C}^T \mathcal{M}^{-1} \mathcal{B}(\mathbf{\Phi}_i) \mathbf{\Phi}_j a_i a_j \\ & + \sum_{i=1}^{R} \mathcal{C}^T \mathcal{M}^{-1} (\mathcal{B}(\overline{\mathbf{U}}) \mathbf{\Phi}_i + \mathcal{B}(\mathbf{\Phi}_i) \overline{\mathbf{U}} + \mathcal{D} \mathbf{\Phi}_i) a_i \\ & + \mathcal{C}^T \mathcal{M}^{-1} (\mathcal{B}(\overline{\mathbf{U}}) \overline{\mathbf{U}} + \mathcal{D} \overline{\mathbf{U}}) \end{aligned}$$

From this equation we can deduce that P^R can be decomposed as a linear combination of partial pressures,

$$P^R = \sum_{i,j=1}^{R} P_{ij}^R a_i a_j + \sum_{i=1}^{R} P_i^R a_i + P_0^R, \tag{3.9}$$

where the partial pressures satisfy

$$\begin{aligned} -\mathcal{C}^T \mathcal{M}^{-1} \mathcal{C} P_{ij}^R &= \mathcal{C}^T \mathcal{M}^{-1} \mathcal{B}(\mathbf{\Phi}_i) \mathbf{\Phi}_j, \\ -\mathcal{C}^T \mathcal{M}^{-1} \mathcal{C} P_i^R &= \mathcal{C}^T \mathcal{M}^{-1} (\mathcal{B}(\overline{\mathbf{U}}) \mathbf{\Phi}_i + \mathcal{B}(\mathbf{\Phi}_i) \overline{\mathbf{U}} + \mathcal{D} \mathbf{\Phi}_i), \\ -\mathcal{C}^T \mathcal{M}^{-1} \mathcal{C} P_0^R &= \mathcal{C}^T \mathcal{M}^{-1} (\mathcal{B}(\overline{\mathbf{U}}) \overline{\mathbf{U}} + \mathcal{D} \overline{\mathbf{U}}). \end{aligned}$$

This means, we have to compute the solution of these $R^2 + R + 1$ systems of linear algebraic equations once, store the resulting partial pressures, and then we can compute the pressure fields associated with the reduced velocities cheaply using (3.9).

3.5 Application to LES using updated coefficients

In this section we provide a reduced-order model that is based on the governing equations of a large-eddy simulation instead of the equations of a direct numerical simulation. The method is not a reduced-order model in the strong sense, however, because its on-line computation time is dependent on the number of unknowns of the original simulation, the reason being the non-linearity in the eddy viscosity model.

We perform a Galerkin projection of the spatially semi-discretized weak form of the LES momentum equations on the $\boldsymbol{\Phi}_1,\ldots,\boldsymbol{\Phi}_R$. The resulting system of ordinary differential equations is given by

$$\sum_{i=1}^{R} A_{ri}\dot{a}_i = \sum_{i,j=1}^{R} B_{rij}a_i a_j + \sum_{i=1}^{R} C_{ri}^{\mathrm{t}}(\mathbf{U}^R)a_i + D_r^{\mathrm{t}}(\mathbf{U}^R), \quad r=1,\ldots,R,$$

where the solution dependent model coefficients are given as

$$C_{ri}^{\mathrm{t}}(\mathbf{U}^R) = \boldsymbol{\Phi}_r^T\mathcal{B}(\overline{\mathbf{U}})\boldsymbol{\Phi}_i + \boldsymbol{\Phi}_r^T\mathcal{B}(\boldsymbol{\Phi}_i)\overline{\mathbf{U}} + \boldsymbol{\Phi}_r^T\mathcal{D}(\mathbf{U}^R)\boldsymbol{\Phi}_i, \quad r,i=1,\ldots,R$$
$$D_r^{\mathrm{t}}(\mathbf{U}^R) = \boldsymbol{\Phi}_r^T\mathcal{B}(\overline{\mathbf{U}})\overline{\mathbf{U}} + \boldsymbol{\Phi}_r^T\mathcal{D}(\mathbf{U}^R)\overline{\mathbf{U}}, \quad r=1,\ldots,R.$$

For linear finite elements the turbulent viscosity ν_{t} is constant within each grid cell. In this case, the expressions for the solution dependent model coefficients can be reformulated, so that the computational cost for computing them reduces to the time needed for constructing ν_{t} from the current solution of the reduced-order model plus R^2+R inner products of vectors whose length is equal to the number of grid cells. To save more computing time, we can extrapolate the solution-dependent coefficients over a short time period before updating them. To this end, we choose a sequence of update times. During the time integration, at the update times we compute and store the coefficients, and between the update times we reconstruct the coefficients by quadratic extrapolation using previously stored values. For the first time steps, where we do not have enough data for a quadratic extrapolation, we use a full computation of the coefficients for each evaluation of the right-hand side [E4].

3.6 Application to LES using calibration

In this section we formulate a reduced-order model for LES that has the same on-line computational cost as the standard reduced-order model based on a direct simulation of the incompressible Navier-Stokes equations. The method uses a calibration of the model coefficients of the constant and linear terms of the reduced-order model, so that it mimics the behavior of the LES, even if it does not contain the non-linear dynamics of the eddy viscosity model.

Let $a_{r,n} = (\mathbf{U}_n - \overline{\mathbf{U}}, \boldsymbol{\Phi}_r)_{\mathcal{M}}$ and let $\hat{a}_{r,n}$ be the solution of a reduced-order model at t_n, for $r=1,\ldots,R$ and $n=1,\ldots,N$. Here, the number and the placement of the snapshots in time are allowed to differ with respect to the snapshots used to generate the reduced basis functions. Further, let $a_{r,\mathrm{s}}$ and $\hat{a}_{r,\mathrm{s}}$ be respective cubic spline interpolations for $r=1,\ldots,R$, so that

$$\mathbf{U}_{\mathrm{s}}^R = \overline{\mathbf{U}} + \sum_{r=1}^{R} a_{r,\mathrm{s}}\boldsymbol{\Phi}_r, \qquad \hat{\mathbf{U}}_{\mathrm{s}}^R = \overline{\mathbf{U}} + \sum_{r=1}^{R} \hat{a}_{r,\mathrm{s}}\boldsymbol{\Phi}_r.$$

A cost functional that measures the difference between the projected solution and the model solution is given as

$$\mathcal{J} = \int_0^T \| \mathbf{U}_\mathrm{s}^R - \hat{\mathbf{U}}_\mathrm{s}^R \|_{\mathcal{M}}^2 \, \mathrm{d}t = \int_0^T \sum_{i,r=1}^{R} (a_{i,\mathrm{s}} - \hat{a}_{i,\mathrm{s}}) A_{ir} (a_{r,\mathrm{s}} - \hat{a}_{r,\mathrm{s}}) \, \mathrm{d}t.$$

We want to let a gradient-based optimization routine find the model coefficients C_{kl} and D_k, for $k,l = 1,\ldots,R$, that minimize the cost functional. In each step of the optimization routine we have to provide $\mathcal{J}$ and its derivatives with respect to the model coefficients. To compute the derivatives we apply adjoint techniques [25] to our problem. One can derive the expressions

$$\frac{D\mathcal{J}}{DC_{kl}} = \int_0^T \hat{b}_k \hat{a}_l \, \mathrm{d}t, \qquad \frac{D\mathcal{J}}{DD_k} = \int_0^T \hat{b}_k \, \mathrm{d}t,$$

where $\hat{b}_1,\ldots,\hat{b}_R$ are the solutions of the adjoint reduced-order model

$$-\sum_{r=1}^{R} \dot{\hat{b}}_r A_{ri} = \sum_{r,j=1}^{R} \hat{b}_r (B_{rij} + B_{rji}) \hat{a}_j + \sum_{r=1}^{R} (\hat{b}_r C_{ri} + 2A_{ir} (a_{r,\mathrm{s}} - \hat{a}_{r,\mathrm{s}})),$$
$$\hat{b}_i(T) = 0, \qquad i = 1,\ldots,R.$$

While in theory $\hat{a}_1,\ldots,\hat{a}_R$ and $\hat{b}_1,\ldots,\hat{b}_R$ are exact solutions of the reduced-order models, in practice they can be replaced by dense output or spline interpolations of a numerical solution.

In each iteration of the optimization routine we are given a set of model coefficients, for which we perform the following steps:

1. Solve the reduced-order model forward in time.
2. Solve the adjoint reduced-order model backward in time.
3. Compute the values of the functional and its derivatives.

By using the adjoint of the reduced-order model, the calibration can be done much faster than by using a finite difference approximation of the gradients of the cost functional, as the computational cost in each step of the optimization is mainly one forward and one backward solution.

3.7 Results for laminar vortex-shedding flow

The accuracy of the reduced-order models was studied for a two-dimensional simulation of a flow around a circular cylinder at a Reynolds number of $Re = 100$. The domain with boundary conditions is sketched in Figure 5, where Γ_N^i denotes Neumann conditions and Γ_D^i denotes Dirichlet conditions for u^i.

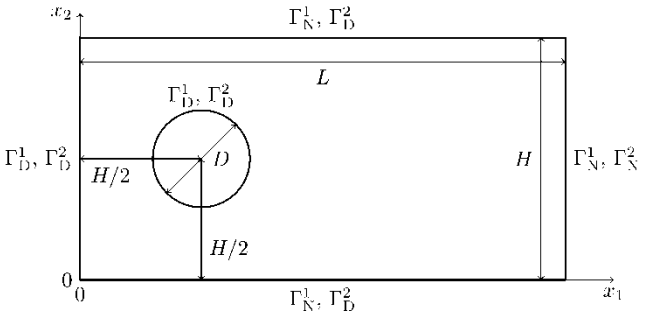

Figure 5: Sketch of the geometry (not to scale) and boundary conditions of the two-dimensional flow around a circular cylinder.

We used the geometric parameters $D_{\text{cyl}} = 0.1\,\text{m}$, $L = 3\,\text{m}$ and $H = 2\,\text{m}$, the inflow velocity was set to $u_{\text{in}} = 1\,\text{m/s}$ and the kinematic viscosity was set to $\nu = 0.001\,\text{m/s}^2$. The simulation was performed with the finite element solver Kardos [E5], using stabilized linear finite elements [E6] and the ROS3P time integration method [E7]. For the spatial discretization we used a triangular mesh with 79723 mesh nodes, locally refined near the cylinder. The time was discretized with a constant step size of $\Delta t = 0.001\,\text{s}$, but only every tenth solution was stored. The simulation was started with a fluid at rest. After a transient simulation time of less than $20\,\text{s}$ the solution became periodic. A snapshot of the solution at $t = 20\,\text{s}$ is presented in Figure 6, which demonstrates the appearance of a regularly shaped von Kármán vortex street.

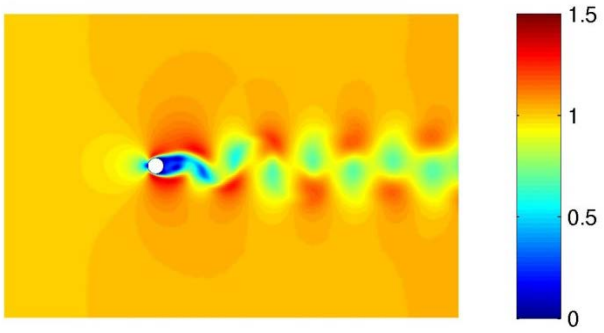

Figure 6: First snapshot of the absolute velocity field of the two-dimensional numerical solution.

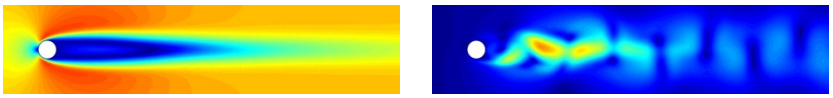

Figure 7: Central part of the absolute velocity field of the reference flow, sampled at t=3.89 s (left). Snapshot fluctuation at t=20 s with respect to the reference flow (right). The same color scale as in Figure 6 is used for both images.

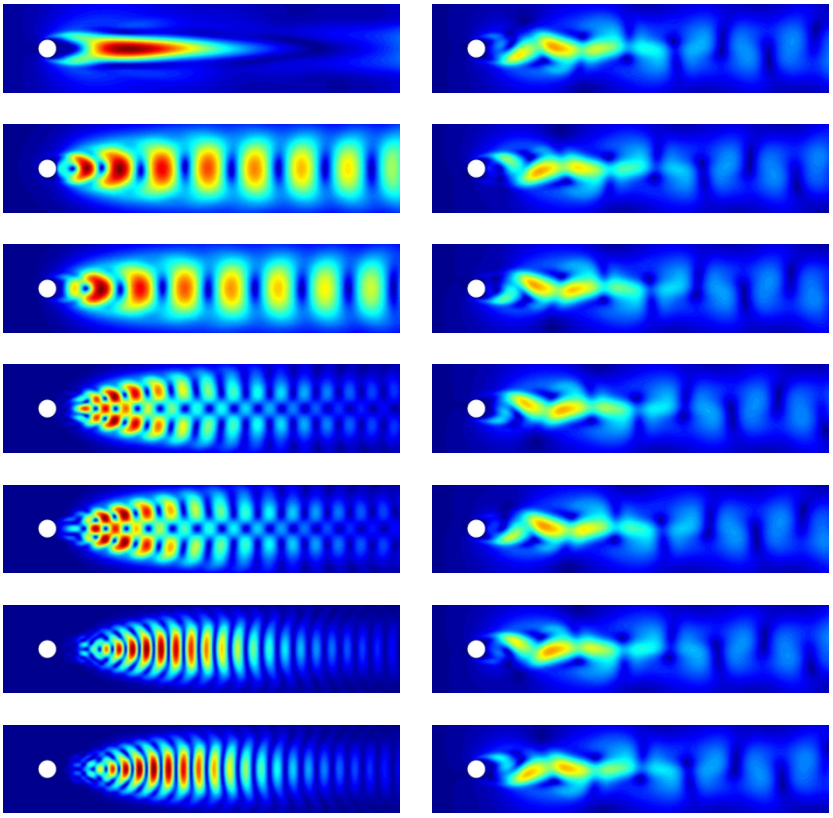

Figure 8: Modes of a POD (left) of rank 7 and a CVT (right) of rank 7. The plots show the absolute values of the modal vector fields.

We chose the snapshot at $t = 3.89\,\mathrm{s}$ as a reference flow $\bar{\mathbf{U}}$, which is shown in Figure 7 together with the snapshot fluctuation at $t = 20\,\mathrm{s}$ with respect to the reference flow. Note that only a cut-out of the domain is plotted in Figure 7 and in the following figures. Using the snapshot fluctuations at times $t = 20.00\,\mathrm{s}, 20.01\,\mathrm{s}, \ldots, 20.58\,\mathrm{s}$, corresponding to one shedding cycle, we created sets of POD and CVT reduced basis functions. Figure 8 displays the reduced basis functions of a 7 mode POD and a 7 mode CVT.

To compare the snapshots with their reduced-order representations a few definitions are required: Let a set of POD or CVT reduced basis functions $\boldsymbol{\Phi}_1, \ldots, \boldsymbol{\Phi}_R$ be given for some fixed rank R. Let $\mathbf{U}_1, \ldots, \mathbf{U}_N$ and $P_1, \ldots, P_N$ be velocity and pressure solution vectors, respectively, sampled at $t_1, \ldots, t_N$. These solution vectors may be different from the snapshots with which the reduced basis functions were created. Using the reduced-order coefficients

$$a_{r,n} = (\mathbf{U}_n - \bar{\mathbf{U}}, \boldsymbol{\Phi}_r)_{\mathcal{M}}, \quad n = 1, \ldots, N, \quad r = 1, \ldots, R,$$

we define the reduced-order approximations, based on (3.5) and (3.9), as

$$\mathbf{U}_n^R = \bar{\mathbf{U}} + \sum_{r=1}^{R} a_{r,n} \boldsymbol{\Phi}_r, \quad n = 1, \ldots, N,$$

$$P_n^R = \sum_{i,j=1}^{R} P_{ij}^R a_{i,n} a_{j,n} + \sum_{i=1}^{R} P_i^R a_{i,n} + P_0^R, \quad n = 1, \ldots, N.$$

We used the reference flow shown in Figure 7 and the reduced basis functions shown in Figure 8 to approximate the velocity field from time $t = 20\,\mathrm{s}$ to time $t = 21\,\mathrm{s}$. We chose a monitoring point $\mathbf{x}_m = (1.2, 1)$ in the wake of the flow. In Figure 9 the time dependent streamwise velocity component at the monitoring point is compared to the reduced-order approximations of rank 7. The POD and CVT basis functions have lead to different approximations at the monitoring point, but the approximation quality was similar.

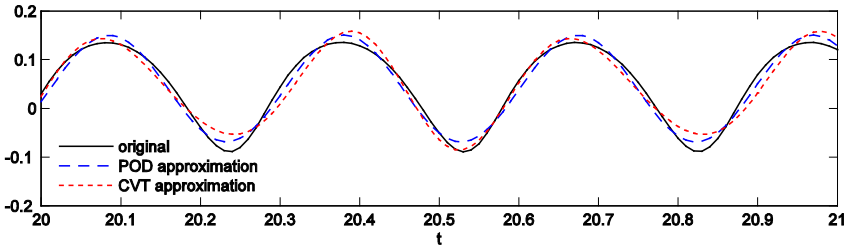

Figure 9: Comparison of the velocity components u_1 at the monitoring point $\mathbf{x}_m = (1.2, 1)$ for the original simulation, the POD approximation of rank 7 and the CVT approximation of rank 7.

To compare the solutions of the reduced-order model with the reduced-order approximations, we denote the numerical solutions of the reduced-order model at times $t_1,\ldots,t_N$ as $\hat{a}_{r,n}$ for $r=1,\ldots,R$ and $n=1,\ldots,N$. We define the reduced-order modeled velocity and pressure fields, based on (3.5) and (3.9) as

$$\hat{\mathbf{U}}_n^R = \bar{\mathbf{U}} + \sum_{r=1}^{R} \hat{a}_{r,n}\boldsymbol{\Phi}_r, \quad n=1,\ldots,N,$$

$$\hat{P}_n^R = \sum_{i,j=1}^{R} P_{ij}^R \hat{a}_{i,n}\hat{a}_{j,n} + \sum_{i=1}^{R} P_i^R \hat{a}_{i,n} + P_0^R, \quad n=1,\ldots,N.$$

Now we define, for $n=1,\ldots,N$, the L^2 model, approximation and total errors, respectively, as

$$E_{n,R}^{\mathbf{U},\mathrm{m}} = \| \hat{\mathbf{U}}_n^R - \mathbf{U}_n^R \|_{\mathcal{M}},$$

$$E_{n,R}^{\mathbf{U},\mathrm{a}} = \| \mathbf{U}_n^R - \mathbf{U}_n \|_{\mathcal{M}},$$

$$E_{n,R}^{\mathbf{U},\mathrm{t}} = \| \hat{\mathbf{U}}_n^R - \mathbf{U}_n \|_{\mathcal{M}}.$$

We also measure the errors in the drag force F_{D} and the lift force F_{L} acting on the cylinder. These forces are given as

$$F_{\mathrm{D}}(p,\mathbf{u}) = \int_S \left(p n_1 - \nu \left(\nabla u_1 + \partial_{x_1}\mathbf{u} \right) \cdot \mathbf{n} \right) \mathrm{d}S,$$

$$F_{\mathrm{L}}(p,\mathbf{u}) = \int_S \left(p n_2 - \nu \left(\nabla u_2 + \partial_{x_2}\mathbf{u} \right) \cdot \mathbf{n} \right) \mathrm{d}S,$$

where S is the surface of the cylinder and $\mathbf{n}$ points outside of the domain. By using the finite element approximations of p and $\mathbf{u}$ we can write the drag and lift forces as functions of the nodal vectors, $F_{\mathrm{D}}(P,\mathbf{U})$ and $F_{\mathrm{L}}(P,\mathbf{U})$, respectively. Now we define the drag model, approximation and total errors, respectively, as

$$E_{n,R}^{\mathrm{D},\mathrm{m}} = F_{\mathrm{D}}(\hat{P}_n^R, \hat{\mathbf{U}}_n^R) - F_{\mathrm{D}}(P_n^R, \mathbf{U}_n^R),$$

$$E_{n,R}^{\mathrm{D},\mathrm{a}} = F_{\mathrm{D}}(P_n^R, \mathbf{U}_n^R) - F_{\mathrm{D}}(P_n, \mathbf{U}_n),$$

$$E_{n,R}^{\mathrm{D},\mathrm{t}} = F_{\mathrm{D}}(\hat{P}_n^R, \hat{\mathbf{U}}_n^R) - F_{\mathrm{D}}(P_n, \mathbf{U}_n).$$

The lift errors are defined in an analogous way. To measure the errors over all time steps we use the error norm

$$\| E_R \| = \sqrt{\sum_{n=1}^{N} E_{n,R}^2},$$

where $E_{n,R}$ can be any of the L^2, drag or lift errors defined above.

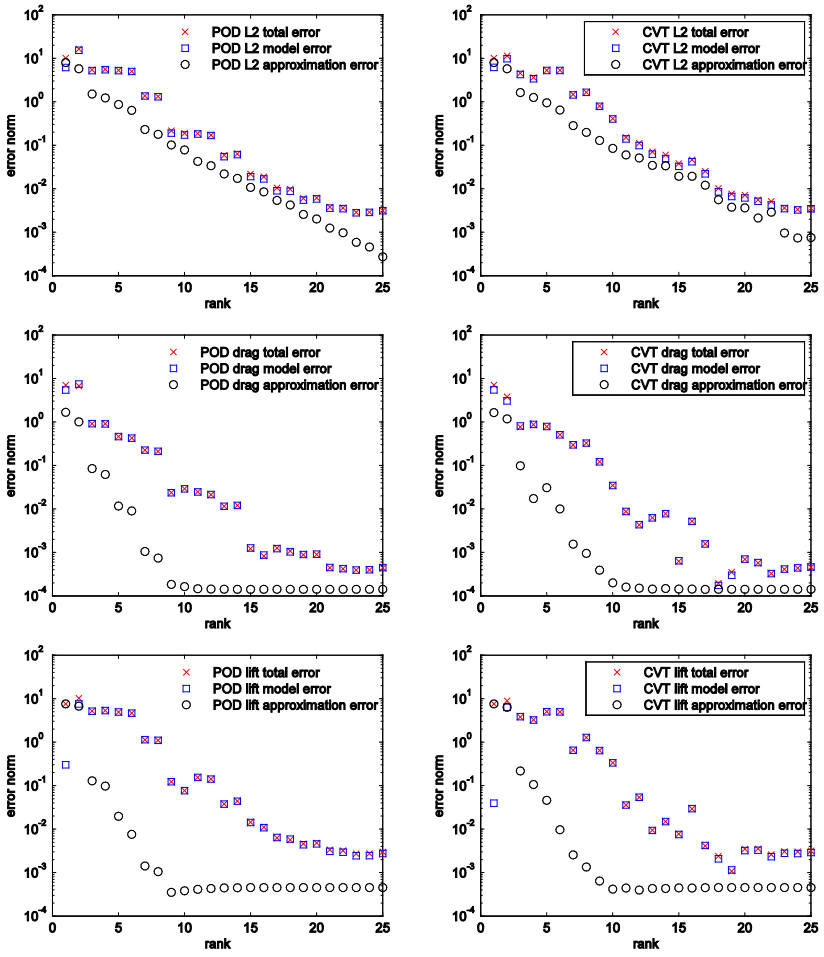

Figure 10: Errors norms, depending on the rank of the reduced bases, using POD (left) and CVT (right) basis functions. From top to bottom: L^2 velocity error, drag error, lift error.

We created POD and CVT reduced-order models of the cylinder flow simulation, using the snapshots at $t = 20.00\,\text{s}, 20.01\,\text{s}, \ldots, 20.58\,\text{s}$ and the reference flow at $t = 3.89\,\text{s}$. The ranks R of the reduced bases were varied from 1 to 25. Reduced-order approximations and model solutions were computed within the larger time interval $t \in [20, 30]$ and compared to the snapshots in the same interval.

The respective L^2 velocity errors and the drag and lift errors are presented in Figure 10. It turns out that the POD and CVT models behave qualitatively similar.

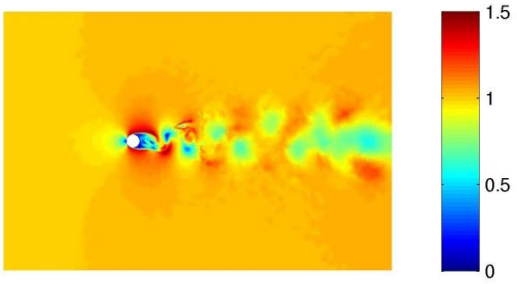

Figure 11: First snapshot of the absolute Smagorinsky-filtered velocity field of a three-dimensional large-eddy simulation.

In the L^2 case the modeling error is relatively close to the approximation error, which means that the reduced-order model is nearly optimal. Around $R = 25$, however, the modeling error stops to decrease any further. By comparing different mesh and time step sizes of the original simulations it could be verified that this accuracy limit of the reduced-order model is determined by the numerical errors of the snapshots. For the drag and lift computations, the approximation error first drops rapidly and then stays nearly constant for $R \geq 10$. This behavior can be explained by the fact that the reduced-order approximation of the pressure field was not obtained by a projection, but by solving a set of pressure Poisson equations. The computation of the snapshots, however, did not involve a pressure Poisson equation, so even the reduced-order approximations of the drag and lift forces contain some modeling error.

3.8 Results for turbulent flow

In this section we study the accuracy of the reduced-order models for a three-dimensional large-eddy simulation performed with the finite element software Kardos [E5]. The domain was obtained by extruding the two-dimensional geometry of the preceding section in the third dimension by a depth of $0.3\,\mathrm{m}$. We chose an inflow velocity of $u_{\mathrm{in}} = 1\,\mathrm{m/s}$ and a kinematic viscosity of $1/39000\,\mathrm{m/s}^2$, so that the Reynolds number became $Re = 3900$. For the modeling of the turbulent stress tensor we used a Smagorinsky constant of $C_{\mathrm{S}} = 0.15$. The tetrahedral mesh was manually refined near the cylinder and in the near-cylinder wake region, resulting in a number of 123553 mesh nodes. For the time discretization a constant step size of $0.002\,\mathrm{s}$ was chosen. The initial velocity field was taken from a simulation that was performed with an adaptive time stepping, starting from a fluid at rest and running through the transient flow phase until a developed turbulent flow was reached. A snapshot of the initial velocity field is shown in Figure 11.

Figure 12: Central part of the absolute velocity field of the reference flow (left). Central part of the absolute velocity field of the fluctuation based on the reference flow and the first snapshot (right).

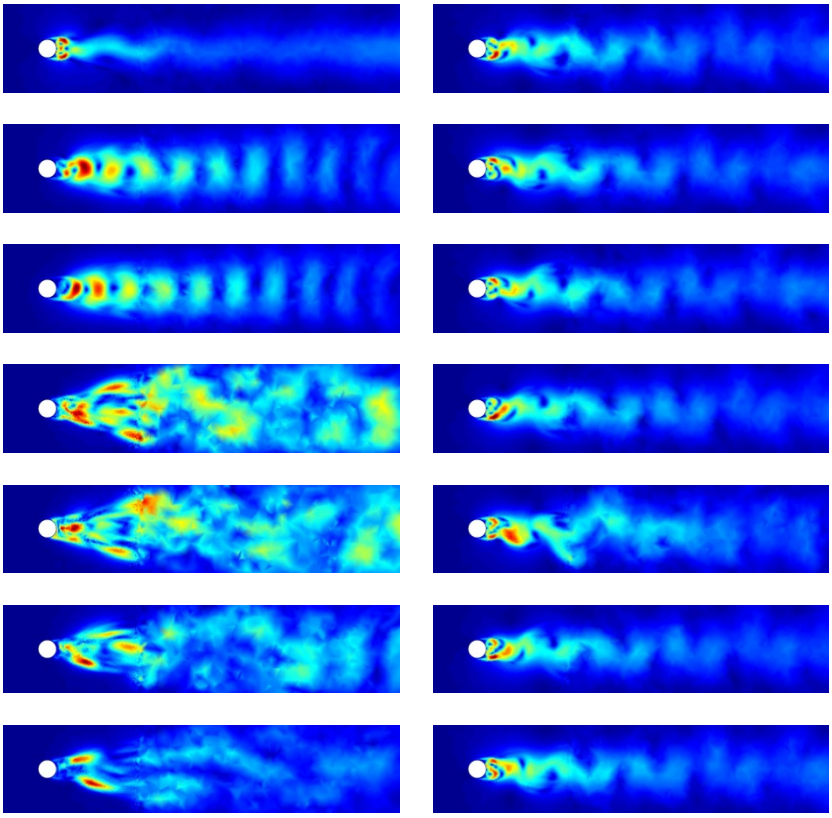

Figure 13: Modes of a velocity POD (left) of rank 7 and a velocity CVT (right) of rank 7. The plots show the absolute values of the vector fields.

After computing the solution of the LES within a time interval of $4\,\mathrm{s}$, we selected the 1000 available LES solutions from $t_1 = 0\,\mathrm{s}$ to $t_{1000} = 1.998\,\mathrm{s}$ as snapshots and picked a solution from the transient start-up simulation as a reference flow. In Figure 12 the reference velocity field and a velocity fluctuation around the reference are shown. The reason for not including all available numerical solutions up to $t = 4\,\mathrm{s}$ in the snapshot data base was to enable the assessment of the reduced-order models with respect to reproducing `known' snapshots compared to reproducing `unknown' snapshots. While the first case is a necessary premise for the success of the methods, the latter case will be more significant for real-life applications, where the reduced model is to be used as a surrogate for the original model.

The snapshot fluctuations around the reference flow were used to generate POD and CVT reduced basis functions. In Figure 13 the reduced basis functions of a 7 mode POD are compared with a 7 mode CVT.

As a visual criterion for the comparison of the different reduced-order models for large-eddy simulations we took the time evolution of the streamwise velocity component at the monitoring point $(1.2, 1, 0.15)$ from $t = 0\,\mathrm{s}$ up to $t = 4\,\mathrm{s}$. In Figure 14 the different reduced-order solutions of rank 64 are compared to the original simulation results.

In the first plot of Figure 14, the projection of the solution on the reduced-basis functions is shown, which serves as a reference for the other models, as the projection is the L^2 optimal approximation of the original velocity field by a linear combination of the chosen reduced-basis functions. It can be observed that the first half of the snapshots, which formed the snapshot data base for building the reduced basis functions, are approximated well by the projected snapshots, while the other half is approximated poorly. The difference between the projection on the POD and on the CVT basis functions is relatively small over the whole time interval.

The second plot of Figure 14 shows the solution of the DNS reduced-order models applied to the LES test case. The model solutions quickly diverge from the original simulation results and exhibit strong oscillations. The results of the POD and CVT are different, but qualitatively similar.

The solution of the models with updated coefficients, based on the governing equations of the LES, is shown in the third plot of Figure 14. The model coefficients were updated at every 10th snapshot time. While the models are able to capture the dynamics of the snapshot phase well, they fail to approximate the dynamics of the unknown phase, due to the inability of the reduced basis functions to approximate these solutions. The accuracies of the POD and CVT models are similar.

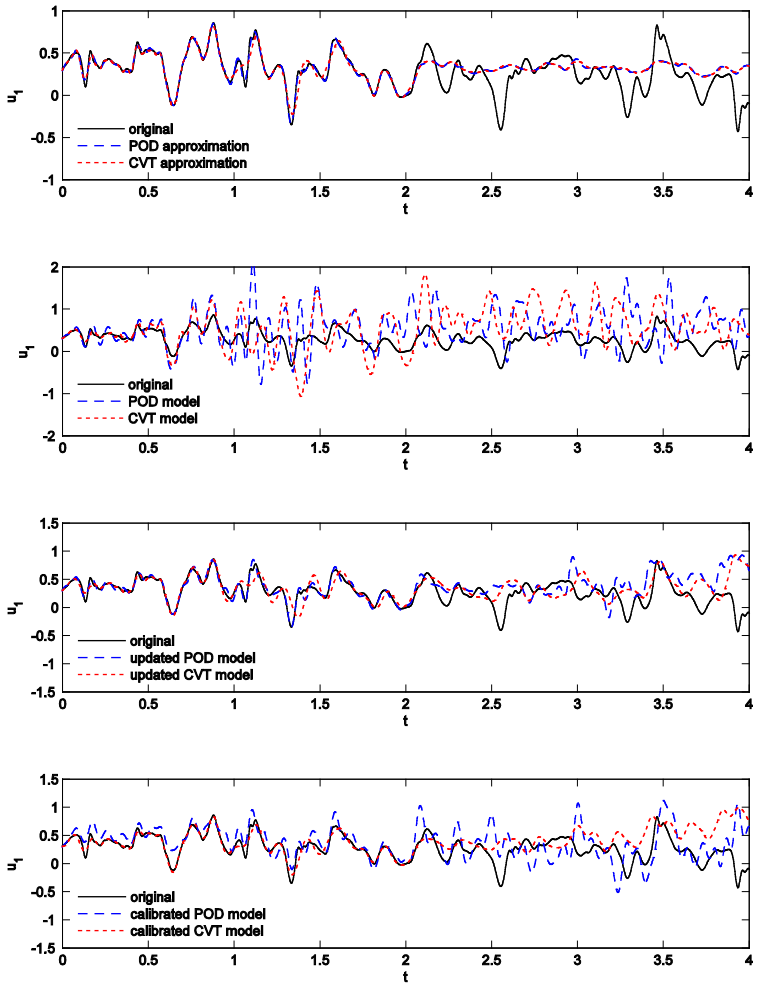

Figure 14: Comparison of the streamwise velocity component u_1 of the original simulation with the POD and CVT reduced-order solutions of rank 64 at the monitoring point $\mathbf{x} = (1.2, 1, 0.15)$. For $t \geq 2$, the solutions are not contained in the snapshot data base used for constructing the reduced basis function. From top to bottom: projection of the velocity on the reduced basis functions, solution of reduced DNS model, solution of the reduced LES model, solution of the reduced DNS model calibrated to the snapshot data base.

In the last plot of Figure 14 we show the results of the calibrated models. The models are based on the equations of a direct numerical simulation, but the coefficients were calibrated with respect to the snapshots that were used to generate the basis functions. Within the first half of the time interval the

performance is similar to the LES reduced-order model, in the second half the solutions are less accurate. In the calibrated case, the CVT model is more accurate than the POD model.

Finally, we compare the computation times of the updated and the calibrated models. Creating the updated POD and CVT models of rank 64 from the snapshot set took 1712 s and 3863 s of wall-clock time, respectively, while running the models took 5335 s and 4621 s. Creating the calibrated models took 15301 s and 32588 s for POD and CVT, respectively, but their time integrations took merely 21 s and 26 s. The time integration of the finite element model over the same time interval took almost five weeks. All timings were obtained using one computational core of a 3.0 GHz AMD Opteron processor.

4 Summary and Conclusions

In the first part of this paper we have presented a mesh adaptation method based on LES-specific design criteria in order to improve the quality of statistical flow properties. The heart of the method is an iterative moving mesh strategy that balances statistically averaged values over the whole spatial grid. As a test problem the flow over periodic hills at Re=10595 was considered. Inspired by the remarkably good results for the mean streamwise velocity reported in Hertel et al. [E2], we have combined this quantity with the statistically averaged turbulent kinetic energy and shear stresses within the framework of balanced monitor functions, following the approach developed by van Dam [15]. The key idea is to improve the local resolution of these important LES quantities through a higher concentration of grid points in areas where they are insufficiently resolved.

Based on our numerical experiments for the periodic hill flow we can draw the following main conclusions: (i) Significant improvement compared to the initial grid approximation can be observed for all combinations of LES-specific quantities. (ii) Even though the additional consideration of the turbulent kinetic energy and part of the shear stress to steer the moving mesh approach can locally improve the flow resolution with respect to specific quantities such as the reattachment point, the overall and well balanced quality of the streamwise velocity cannot be beaten. Further studies on different flows are planned for future research.

In the second part of this work, reduced-order models were studied for a laminar direct numerical simulation and a turbulent large-eddy simulation of the flow around a cylinder. The reduced-order models for the velocity fields were obtained by a Galerkin projection of the semi-discretized flow problems onto relatively small sets of global basis functions. The reduced-order models for the pressure fields were derived by using a discrete pressure Poisson equation. Two different methods were used to generate basis functions for the projection, namely the

proper orthogonal decomposition and the centroidal Voronoi tessellation. The solutions of the resulting reduced-order models were compared by their accuracy with respect to the solutions of the underlying finite element simulations.

For the DNS test case, the errors in the reduced-order solutions could be diminished to the order of magnitude of the numerical error of the original finite element solution. These results were possible with using about 25 POD or CVT modes, which validated the applicability and correctness of the models. The POD and CVT results did not differ much with respect to the error in the velocity field and in the time-dependent drag and lift forces. The findings indicate that both methods are similarly suitable for the construction of reduced-order models.

For the LES test case, besides the different types of basis functions, we compared two different approaches for modeling the dynamics: a model based on the LES equations and a calibrated DNS model. Both models succeeded to capture the ‘known’ solutions that were present in the snapshot database used for the creation of the reduced basis functions, but they failed to capture ‘unknown’ solutions that were not present in the snapshot database. As in the laminar case, the differences between the POD and CVT based models turned out to be rather small. Comparing the computational times, running the calibrated models took much less time than running the updated models, but the setup phase of the calibrated models was longer.

The fact that the turbulent reduced-order models could not reproduce `unknown' snapshots highlights an important issue of reduced-order modeling in a turbulent context. While a lot can be done to improve the dynamics of the POD and CVT models, as shown in this work, the output of the models can, by definition, only be a linear combination of snapshots. Therefore a sufficiently large number of snapshots and, consequently, a large number of reduced basis functions must be provided to enable accurate computations of turbulent flows.

Acknowledgements

The authors acknowledge the financial support from the German Research Council (DFG) through the SFB568. We would also like to thank Jochen Fröhlich and Claudia Hertel (TU Dresden) for making the turbulent flow solver LESOCC2 available to us and for their kind programming support during our numerical studies.

References

Project-related Publications

E1. Löbig S., Dörnbrack A., Fröhlich J., Hertel C., Kühnlein Ch., Lang J., Towards large eddy simulation on moving grids, Proc. Appl. Math. Mech. 9, 445-446 (2009)

E2. Hertel C., Schümichen M., Löbig S., Fröhlich J., Lang J., Adaptive large eddy simulation with moving grids. Preprint Technische Universität Dresden (2011), submitted to Theoretical and Computational Fluid Dynamics

E3. Lang J., Cao W., Huang W., Russell R.D., A two-dimensional moving finite element method with local refinement based on a posteriori error estimates, Applied Numerical Mathematics 46:75-94 (2003)

E4. Ullmann S., Lang J., A POD-Galerkin reduced model with updated coefficients for Smagorinsky LES, In: Pereira J.C.F., Sequeira A., Pereira J.M.C. (eds), Proceedings of the V European Conference on Computational Fluid Dynamics ECCOMAS CFD 2010, Lisbon, Portugal (2010)

E5. Erdmann B., Lang J., Roitzsch R., Kardos user's guide. ZIB-Report 02-42, ZIB (2002)

E6. Lang J., Adaptive incompressible flow computations with linearly implicit time discretization and stabilized finite elements. In: Papailiou K., Tsahalis D., Periaux J., Hirsch C., Pandolfi M. (eds) Computational Fluid Dynamics '98 (1998)

E7. Lang J., Verwer J., ROS3P—an accurate third-order Rosenbrock solver designed for parabolic problems, BIT Numerical Mathematics 41:730-737 (2001)

Other Publications

1. Huang W., Russell R.D., Adaptive Moving Mesh Methods, 1st edn., Springer New York (2011)
2. Hertel C., Fröhlich J., Error reduction in LES via adaptive moving grids, QLES II, Pisa, Italien, 9.-11 Sep. 2009, Proc.: M.-V. Salvetti et al. (Hsg.), Quality and Reliability of Large-Eddy Simulations II, Springer (2009)
3. Holmes P., Lumley J., Berkooz G., Turbulence, Coherent Structures, Dynamical Systems and Symmetry, Cambridge University Press (1996)
4. Sirovich L., Turbulence and the dynamics of coherent structures, parts I, II and III, Quarterly of Applied Mathematics 45:561-571 (1987)
5. Rempfer D., On low-dimensional Galerkin models for fluid flow, Theoretical and Computational Fluid Dynamics 14(2):75-88 (2000)
6. Bergmann M., Bruneau C., Iollo A., Enablers for robust POD models, Journal of Computational Physics 228(2):516-538 (2009)

7. Telib H., Manhart M., Iollo A., Analysis and low-order modeling of the inhomogeneous transitional flow inside a T-mixer, Physics of Fluids, 16:2717-2731 (2004)
8. Buffoni M., Camarri S., Iollo A., Salvetti M., Low-dimensional modelling of a confined three-dimensional wake flow, Journal of Fluid Mechanics 569:141-150 (2006)
9. Couplet M., Basdevant C., Sagaut P., Calibrated reduced-order POD-Galerkin system for fluid flow modeling, Journal of Computational Physics 207:192-220 (2005)
10. Wang Z., Akhtar I., Borggaard J., Iliescu T., Two-level discretizations of nonlinear closure models for proper orthogonal decomposition. Journal of Computational Physics 230:126-146 (2011)
11. Du Q., Faber V., Gunzburger M., Centroidal Voronoi tessellations: applications and algorithms. SIAM Review 41(4):637-676 (1999)
12. Burkardt J., Gunzburger M., Lee H.C., POD and CVT-based reduced-order modeling of Navier-Stokes flows, Computer Methods in Applied Mechanics and Engineering 196(1-3):337-355 (2006)
13. Smagorinsky J., General circulation experiments with the primitive equations, I, The basic experiment. Monthly Weather Review, 91:99-164 (1963)
14. Winslow A.M., Numerical solution of the quasilinear poisson equation in a nonuniform triangle mesh, Journal of Computational Physics 2:149-172 (1967)
15. van Dam A., Go with the flow, Ph.D. Thesis, Utrecht University (2009)
16. Ferziger J.H., Peric M., Computational Methods for Fluid Dynamics, 3rd edn., Springer Verlag (2002)
17. Demirdzic I., Peric M., Space conservation law in finite volume calculations of fluid flow, International Journal for Numerical Methods in Fluids 8:1037-1050 (1988)
18. Stone H.L., Iterative solution of implicit approximation of multidimensional partial differential equations, SIAM Journal on Numerical Analysis 5:530-558 (1968)
19. Fröhlich J., Mellen C.P., Rodi W., Temmermann L., Leschziner M.A., Highly resolved large-eddy simulation of separated flow in a channel with streamwise periodic constrictions, Journal of Fluid Mechanics 526:19-66 (2005)
20. Berselli L., Iliescu T., Layton M., Mathematics of Large Eddy Simulation of Turbulent Flows, 1st edn., Springer-Verlag Heidelberg Berlin (2006)
21. Lloyd S.P., Least squares quantization in PCM, IEEE Transactions on Information Theory 28(2):129-137 (1982)
22. Rempfer D., Investigations of boundary layer transition via Galerkin projection on empirical eigenfunctions, Physics of Fluids 8(1):175-188 (1996)
23. Noack B., Papas P., Monkewitz P.A., The need for a pressure-term representation in empirical Galerkin models of incompressible shear flows, Journal of Fluid Mechanics 523:339-365 (2005)

24. Gresho P.M., Sani R.L., Incompressible Flow and the Finite Element method, John Wiley & Sons (2000)
25. Gunzburger M., Perspectives in Flow Control and Optimization, Society for Industrial and Applied Mathematics (2003)